Joule

CellPress
OPEN ACCESS

Article

Decoupling, quantifying, and restoring aging-induced Zn-anode losses in rechargeable aqueous zinc batteries

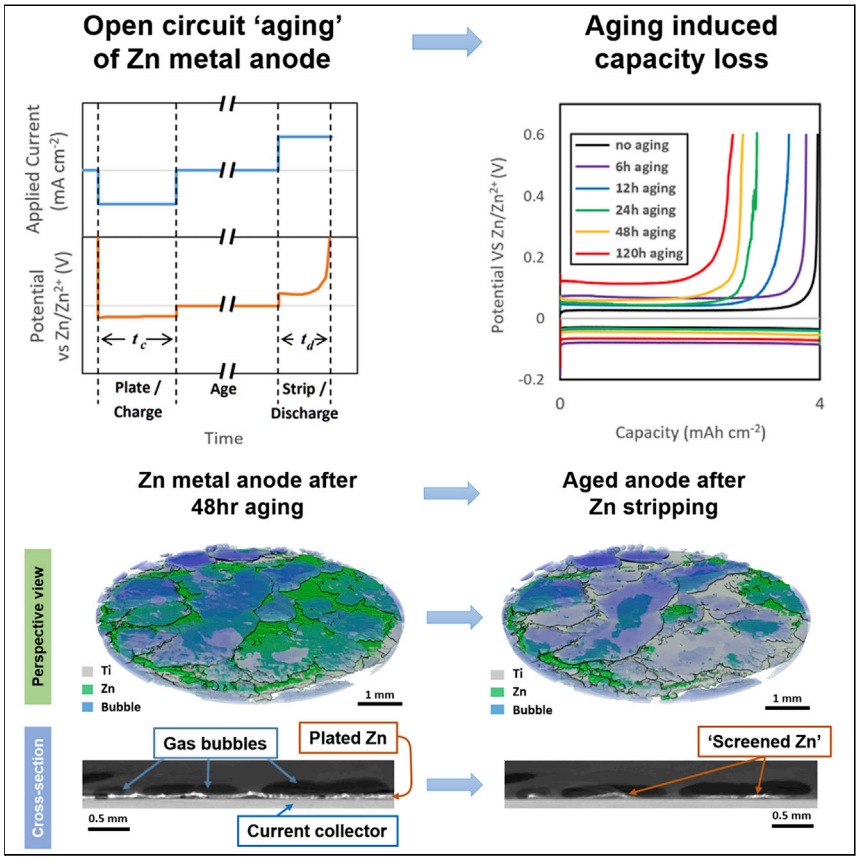

We reveal the crucial role of evolved gas in capacity loss in rechargeable aqueous zinc batteries, which builds up during aging when the cell is not cycled. The zinc-metal anode evolves gas due to corrosion reactions, physically displacing the electrolyte and "screening" the anode. This loss is recoverable by removing the accumulated gas from the cell.

Shengda D. Pu, Bingkun Hu, Zixuan Li, ..., Xiangwen Gao, Peter G. Bruce, Alex W. Robertson

shengda.pu@materials.ox.ac.uk (S.D.P.)
xiangwen.gao@materials.ox.ac.uk (X.G.)
peter.bruce@materials.ox.ac.uk (P.G.B.)
alex.w.robertson@warwick.ac.uk (A.W.R.)

Highlights

Identify the contribution of "open circuit" aging to zinc-metal anode loss

Delineate and quantify the mechanisms that contribute to this aging

Operando X-ray tomography shows the importance of gas evolution

Capacity loss is recoverable by removing the accumulated gas

Pu et al., Joule 7, 366–379
February 15, 2023 © 2023 The Author(s).
Published by Elsevier Inc.
https://doi.org/10.1016/j.joule.2023.01.010

CellPress
OPEN ACCESS

Joule

Article

Decoupling, quantifying, and restoring aging-induced Zn-anode losses in rechargeable aqueous zinc batteries

Shengda D. Pu,[1,5,*] Bingkun Hu,[1,5] Zixuan Li,[1,5] Yi Yuan,[1] Chen Gong,[1] Ziyang Ning,[1] Chloe Chau,[1] Sixie Yang,[1] Shengming Zhang,[1] Liquan Pi,[1] Yuanbo T. Tang,[1] Jili Yue,[1,2] T. James Marrow,[1] Xiangwen Gao,[1,*] Peter G. Bruce,[1,3,*] and Alex W. Robertson[4,6,*]

SUMMARY

Rechargeable aqueous zinc batteries offer low cost, safety, and good cycling capacity, largely due to the water-compatible Zn-metal anode. However, Zn anodes corrode in aqueous electrolytes. While such corrosion is well known, distinguishing the relative importance of corrosion contributions toward anode capacity loss remains less understood. Here, by systematically cycling Zn anodes with controlled loading and under different aging conditions, we successfully decouple and quantify the aging-induced contributions toward anode degradation in mildly acidic aqueous electrolytes. While some losses occur due to the irreversible consumption of Zn into corrosion by-products, we demonstrate that the bigger contributor to this efficiency loss (over 80%) is the physical screening effect of evolved gases, preventing the reversible dissolution of deposited Zn. Understanding the crucial role of evolved gas during cell aging, and how it can accumulate and effectively passivate large sections of the battery anode, will have important implications in the development of rechargeable aqueous zinc batteries.

INTRODUCTION

The aqueous zinc battery (AZB) is a rechargeable battery that offers low cost, low toxicity, and ease of handling, while also exhibiting good volumetric capacity.[1–6] Recent advances in neutral and mildly acidic electrolyte systems, in particular zinc sulfate ($ZnSO_4$),[7–12] have offered a new approach to realizing a practical AZB beyond the use of the more established alkaline zinc electrolytes, which often suffer from limited reversibility.[8,13,14] The critical issues suffered by many rechargeable alkaline AZBs, such as dendrite formation and low cycling efficiency, have been shown to be largely negated by employing mildly acidic or neutral electrolytes, which can demonstrate significantly improve cycling performance.[15–23]

A key advantage of the AZB is the relative stability of its metallic anode. Unlike lithium-metal batteries or other battery systems with highly reactive metallic anodes, the metallic Zn anode can be directly used in aqueous electrolytes. However, it is well known that the Zn anode degrades over prolonged cycling and aging in aqueous electrolyte due to reactions with the water solvent, with the irreversible consumption of Zn into corrosion products and the associated hydrogen-evolution reaction occurring even at open circuit.[15,16,24–28] Approaches to combat this include designing the electrode to suppress dendrite growth, for instance, by using a porous

CONTEXT & SCALE

The search for batteries beyond Li-ion that offer better performance, reliability, safety, and/or affordability has led researchers to explore a diverse array of candidates. The advantages of Zn-ion batteries reside in zinc's relatively low reactivity, raising the prospect of a rechargeable battery with a simple aqueous electrolyte and a cheaper, safer option to the organic electrolytes that must be paired with reactive lithium. However, water still reacts with the zinc in corrosion reactions. These consume zinc, lowering the battery's capacity, and generate gas that accumulates in the sealed cell.

We diagnose the contribution of corrosion to performance decay in zinc batteries and reveal the critical role of gas accumulation in deactivating large sections of electrode, which cripples cell performance. Fortunately, electrodes can be reactivated by removal of the gas, demonstrating the importance of designing future cells that either prevent gas formation or facilitate its safe release.

This is an open access article under the CC BY license (http://creativecommons.org/licenses/by/4.0/).

CellPress
OPEN ACCESS

sponge structure[29,30] or by engineering a robust surface layer over the interface,[31,32] tailoring the electrolyte composition to promote more uniform electroplating,[33–35] and facilitating the preferential exhibition of more favorable planar (002) Zn facets via controlled electrodeposition.[36–38]

Despite the progress in making more robust anodes, the irreversible loss of Zn remains a concern. One strategy employed for accommodating this Zn loss is the use of Zn anodes with excess capacity. Unfortunately, this prevents researchers from distinguishing the contribution of aging reactions to the anode's capacity loss. Such capacity loss is easy to overlook as it is effectively hidden by the excess capacity offered by the metallic anode, which offers a deep zinc reservoir for replenishment of lost capacity. A typical commercial Zn foil of 0.25 mm thick is equivalent to an anode-capacity loading of around 150 mAh cm^{-2}—much higher than that of a practical battery. When paired with a cathode of 1 to 4 mAh cm^{-2} capacity, these full cells' anode-to-cathode (N/P) loading ratio can be as skewed as 150:1, making any Zn-anode capacity loss hardly noticeable in the electrochemistry data, even after prolonged cycling.[39,40]

To achieve a higher energy density for future practical cells, AZBs need to have a lower anode-to-cathode capacity ratio to optimize the anode energy density; indeed, the metal-Zn anode's theoretical specific capacity of 820 mAh g^{-1} (or 5,854 mAh L^{-1})[1–3] can only be fully utilized once a 1:1 anode-to-cathode N/P ratio is reached. Therefore, when studying Zn anodes, it is important to moderate the anode capacity-loading level.[40] By doing so, their degradation processes and capacity loss can also be better tracked and quantified during cycling or aging, as demonstrated in lithium-metal battery studies.[41–43]

Here, we diagnose and quantify the metal-anode losses that occur during aging in mildly acidic zinc sulfate electrolyte. We have decoupled and quantified these processes and their corresponding changes with respect to different charge rates, aging time, and anode loadings. Our investigations revealed the presence of aging-induced "screened Zn," which was found to be a major contributor to capacity fade in acidic AZBs. The formation mechanism for this screened Zn was demonstrated to be distinct from Zn lost due to dendrite formation and detachment—"dead Zn"—and was instead found to be a consequence of the aging-induced corrosion of the anode and accompanying gas formation, as identified by *in situ* X-ray computed tomography (XCT). The excess gas formation was found to accumulate and displace the electrolyte away from areas of the anode surface, "screening" these areas of Zn from dissolution during discharge. Following a simple degassing process it was possible to recover a significant proportion of the capacity lost due to aging, as much of the previously isolated screened Zn had its contact with the electrolyte restored. This study provides a fresh perspective of the aging-induced degradation processes in AZBs, through which improved strategies can be developed to mitigate this problem.

RESULTS

A Zn/Ti coin-cell set-up, similar to Cu/Li cells used in lithium-metal-anode research,[40–42] was used for our study. Mildly acidic 2 M $ZnSO_4$ electrolyte was used in all cases. Ti was used as the current collector as it is highly inert to Zn deposition, as it neither alloys with Zn nor acts as a galvanic cathode such as steel, which greatly accelerates Zn corrosion in water.[44–47] The Ti current collector was first electroplated with 4 mAh cm^{-2} of Zn to serve as the Zn anode (Figure S1).

[1]Department of Materials, University of Oxford, Parks Road, Oxford OX1 3PH, UK

[2]Herbert Gleiter Institute of Materials Science and Engineering, Nanjing University of Science and Technology, Nanjing 210094, China

[3]Department of Chemistry, University of Oxford, South Parks Road, Oxford OX1 3QZ, UK

[4]Department of Physics, University of Warwick, Coventry CV4 7AL, UK

[5]These authors contributed equally

[6]Lead contact

*Correspondence:
shengda.pu@materials.ox.ac.uk (S.D.P.),
xiangwen.gao@materials.ox.ac.uk (X.G.),
peter.bruce@materials.ox.ac.uk (P.G.B.),
alex.w.robertson@warwick.ac.uk (A.W.R.)

https://doi.org/10.1016/j.joule.2023.01.010

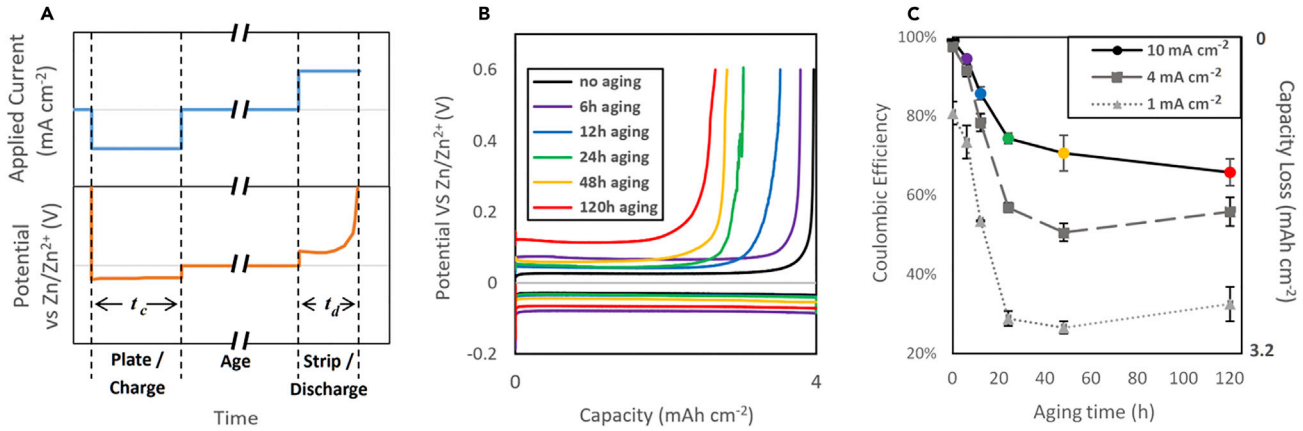

Figure 1. Quantifying aging in zinc-metal anodes

(A) Electrochemical test sequence for quantifying aging-induced capacity loss for Zn/Ti coin cell.

(B) Example charge and discharge curves for cells aged for different lengths of time. The charge and discharge rates were 10 mA cm^{-2}.

(C) Cells' post-aging CE and capacity loss with respect to different aging time and three different charge and discharge rates: 10, 4, and 1 mA cm^{-2}. Each data point is the average from three coin cells, with error bars representing the standard error.

After the Zn electrodeposition, the cells were left to age at ambient conditions for various lengths of time. After aging, the cells were discharged to +0.6 V vs. Zn/Zn^{2+} to strip all the Zn metal left on the anode (Figure 1A). The post-aging reversibility, i.e., the coulombic efficiency (CE) of each cell, can then be calculated based on the time spent to charge, t_c, and time spent to discharge, t_d (Figure 1), defined as:

$$CE = t_d/t_c \times 100\% \quad \text{(Equation 1)}$$

And the anode-capacity loss due to aging, C_{aging}, can be quantified as the capacity difference between charging and discharging, defined as:

$$C_{aging} = \frac{t_c - t_d}{t_c} \times Q_{load} \quad \text{(Equation 2)}$$

where the anode loading Q_{load} = 4 mAh cm^{-2} in this study.

Charging a cell to 4 mAh cm^{-2} at a current density of 10 mA cm^{-2}, followed by immediately discharging it at 10 mA cm^{-2}, i.e., without allowing any aging time, yielded a relatively high reversibility of 99.2%. However, if discharging was left until after 24 h of aging, cells suffered a significant capacity loss of 1.03 mAh cm^{-2} (25.6%). Longer aging times led to further performance decay, with capacity loss of 1.18 mAh cm^{-2} (29.4%) after 48 h of aging and 1.37 mAh cm^{-2} (34.2%) after 120 h of aging (Figure 1B). Similar aging results were obtained with a range of electrolyte concentrations (Figure S2) and were more severe with double separators (Figure S3). This aging-induced capacity loss was more significant in cells that were charged at lower rates; cells cycled at 4 and 1 mA cm^{-2} suffered significantly higher losses of 1.73 (44.1%) and 2.85 mAh cm^{-2} (71.1%), respectively (Figure 1C). This is likely due to the different surface morphology of Zn anodes electroplated under different rates[48]: Zn electroplated at higher current densities exhibits a monolithic crystalline morphology with a low overall surface area (Figure S4C), while Zn plated at lower rates instead deposit as high-surface-area flakes (Figures S4A and S4B). Aging-induced capacity loss was also identified in MnO_2/Zn full cells (Figure S5).

The significant and rapid aging-induced Zn-anode capacity loss presents a significant obstacle for AZBs. Diagnosing the underlying degradation processes that occur

during aging is essential for designing appropriate responses. Previous works have demonstrated that the main degradation processes suffered by a metallic Zn anode in mildly acidic $ZnSO_4$-based AZBs are dendrite formation[17,49–51] and corrosion.[24,26–28,52] Dendrite formation is an electrochemical process that takes place during electroplating and has not been shown to occur spontaneously while simply immersed in electrolyte[17,49–51]; thus it cannot explain the aging-dependency of the observed capacity loss. Corrosion, on the other hand, is known to lead to the formation of zinc hydroxides (ZHO), e.g., $Zn(OH)_2$, and zinc hydroxide sulfate hydrates (ZHS), e.g., $Zn_4SO_4(OH)_6 \cdot xH_2O$,[26–28,52] on the anode surface, with reactions:

$$Zn + 2H_2O \rightarrow Zn(OH)_2 + H_{2(g)}\uparrow \quad \text{(Equation 3)}$$

$$3Zn(OH)_2 + ZnSO_4 \cdot xH_2O \rightarrow Zn_4SO_4(OH)_6 \cdot xH_2O \quad \text{(Equation 4)}$$

The formation of ZHS and ZHO occurs at the cost of the irreversible consumption of metallic Zn (Equations 3 and 4), causing anode-capacity loss. Their presence on the post-aging metallic Zn anodes was confirmed using X-ray photoelectron spectroscopy (XPS) (Figure S6) and X-ray diffraction (XRD), which showed that the relative peak intensity of ZHS and ZHO gradually increased with aging time (Figure S7).

We quantified the irreversible metallic Zn loss due to ZHS/ZHO formation with respect to different aging times by periodically measuring the H_2 evolution via online mass spectroscopy (MS) from a sealed vial cell (Figure S8). It was found that the quantity of ZHS/ZHO increased continuously during aging. Comparing this with the total capacity loss from a coin cell with an equivalent electrode area cycled under identical conditions showed that the ZHS/ZHO formation would be expected to contribute to less than 20% of the total anode capacity loss (Figure 2A); only 0.17 mAh cm^{-2} (compared with 1.31 mAh cm^{-2} total loss) anode Zn loss would be due to ZHS/ZHO formation after the 24-h aging, and only 0.43 mAh cm^{-2} (out of 2.14 mAh cm^{-2} total loss) loss due to ZHS/ZHO formation after the 120-h aging. Cross-section scanning electron microscopy (SEM) imaging and energy dispersive X-ray spectroscopy (EDS) mapping (Figures 2B and S9) of the post-aging Zn anode surface show that only a relatively thin layer of ZHS/ZHO had formed over 120 h of aging, with a thickness of around 4.8 μm. A significant amount of metallic Zn with a thickness of 18.3 μm were preserved after the aging. This corroborates the online MS results and confirms that only a relatively small proportion of the total available Zn was consumed during aging to form ZHS/ZHO. Therefore, it cannot be solely responsible for the aging-induced capacity loss; other processes must contribute.

Upon disassembling the discharged coin cells, a significant amount of residual metallic debris could be found on the Ti current collector and the separators of the aged cells (Figure 2C, red box) while little was found in the unaged cells (Figure 2C, black box). XRD measurements on these aged and stripped anodes identified these residues as mostly Zn metal (Figure 2C). This suggests that parts of the plated-zinc anode, beyond the fraction already converted to ZHS/ZHO and that instead remained metallic, was not electrostripped following the aging process. Unlike the dead Zn that has been reported to become lodged in the separator due to dendrite growth,[53,54] our observed Zn residue correlates strongly with aging; minimal Zn residue was observed in the separator from the cell cycled without aging (Figure 2C, black box), while many Zn residues were observed following aging (Figure 2C, red box). This strong aging dependence suggests that the metal residue cannot be due to dendrite growth and detachment, which occurs independently of aging, and suggests another failure mechanism leading to the isolation of metallic Zn that is more strongly dependent on aging.

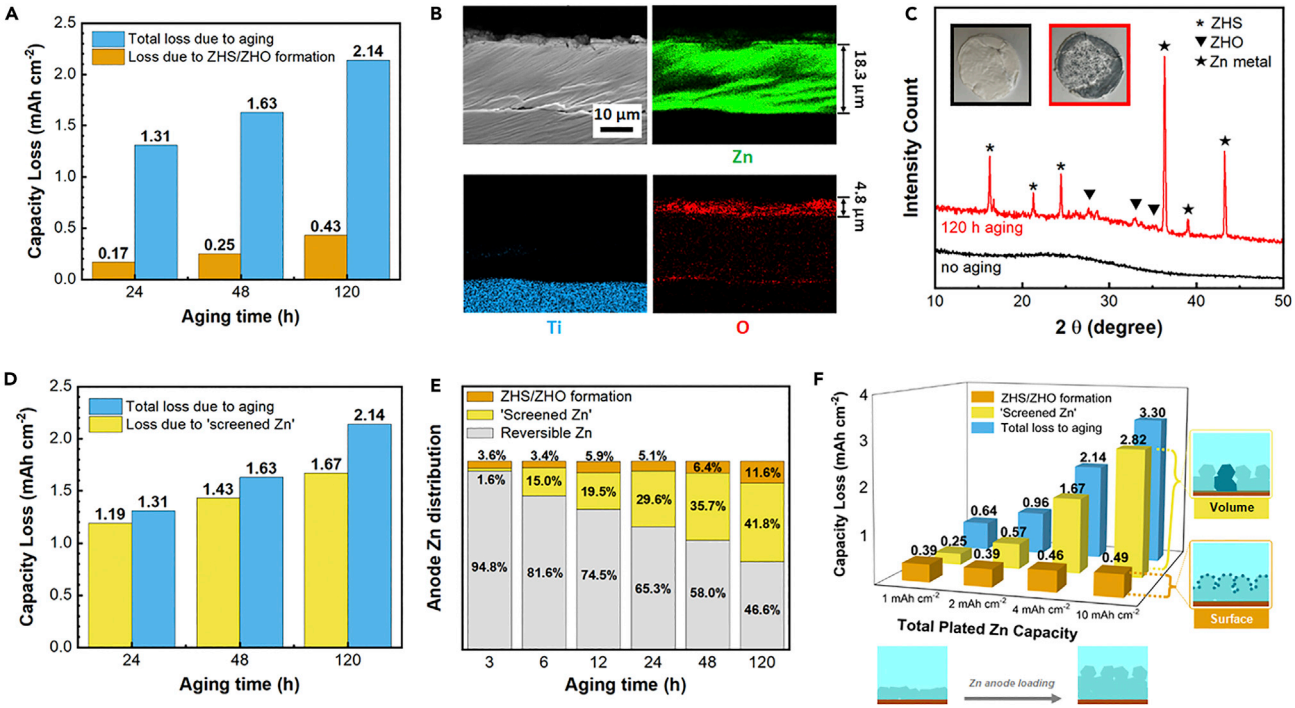

Figure 2. Decoupling the aging-induced loss mechanisms

(A) Comparison of the Zn-anode capacity loss for different aging times due to ZHS/ZHO formation, measured using online MS from a sealed vial cell (see Figure S8), and the total anode loss, measured electrochemically from an equivalent coin cell.

(B) Cross-section SEM imaging and EDS mapping (O, Zn, and Ti) of plated Zn on Ti after 5 days of aging following electroplating to 4 mAh cm^{-2} at 10 mA cm^{-2}. Regions with strong O signal segregation indicates high likelihood of ZHS/ZHO formation.

(C) Photographs and XRD of cell separators following stripping, with 4 mAh cm^{-2} electrodeposition at 10 mA cm^{-2}. Red border, after 5 days of aging; black border, after no aging.

(D) The capacity loss with different aging times due to screened Zn formation (measured by MS of H_2 evolved from H_2SO_4 titrated onto anodes retrieved from the cycled coin cells) and the total anode loss (measured electrochemically from the coin cells).

(E) The distribution of anode Zn after aging between fully reversible Zn, screened Zn, and Zn lost to ZHS/ZHO formation, with respect to aging time.

(F) The total capacity loss with different levels of Zn loading following 5 days of aging.

For (D) and (E) all plating were performed at 10 mA cm^{-2} rate and to 4 mAh cm^{-2} capacity.

The anodes retrieved from the coin cells were titrated with H_2SO_4 solution, and the evolved H_2 was collected and measured, allowing us to quantify the residual metallic Zn in each cell after having undergone aging and electrostripping, as follows:

$$Zn_{(s)} + H_2SO_{4(aq)} \rightarrow ZnSO_{4(aq)} + H_{2(g)}\uparrow \qquad \text{(Equation 5)}$$

Significant amounts of residual metallic Zn were measured for the aged cells, and accounted for over 80% of the total measured aging-induced capacity loss we observed (Figure 2D); an average of 1.19 mAh cm^{-2} (out of 1.31 mAh cm^{-2} total loss) of such residual Zn was detected after 24 h of aging, and 1.67 cm^{-2} (out of 2.14 mAh cm^{-2} total loss) was found after 120 h of aging.

Our MS measurements have shown that the aging-induced capacity loss was mostly due to two degradation processes: (1) Zn loss due to ZHS/ZHO formation (Figure 2A), and (2) the isolation of metallic Zn from the electrochemical dissolution process (Figure 2D). As discussed, while this latter mechanism is similar to the dendrite detachment that leads to dead Zn, it is distinguished by a strong dependence on aging, and so we refer to it here as screened Zn due to its being apparently screened from dissolution during electrostripping. Capacity loss to both ZHS/ZHO formation and

screened Zn isolation took place continuously during aging, leading to increasingly compromised Zn-anode reversibility with longer aging times. Between the two, the screened Zn is the more significant contributor to capacity loss, a trend that becomes especially notable after longer aging time (Figure 2E).

We explored the relative impact of cell aging on anodes primed with various Zn capacities. Four Zn-anode loads were studied, charged with capacities of 1, 2, 4, and 10 mAh cm^{-2}, and all plated at a rate of 10 mA cm^{-2}. As before, after aging these cells were discharged at 10 mA cm^{-2} until reaching a voltage threshold of +0.6 V vs. Zn/Zn^{2+}. It was found that the capacity lost to screened Zn formation continued to increase in cells with higher anode loading (Figure 2F, yellow bars); however the ZHS/ZHO loss increased only slightly as the Zn loading capacity was ramped up (Figure 2F, orange bars). The weak dependence on Zn loading for ZHS/ZHO formation is expected, as it is an interfacial reaction between the metallic Zn anode and the $ZnSO_4$ electrolyte, which is therefore solely dependent on the interfacial surface area (i.e., the anode surface area) and is thus independent of the thickness of the loaded Zn; higher plating capacities lead to a relatively small change in Zn surface area, instead serving to simply thicken the Zn layer deposited on the current collector. The contrasting behavior in the quantity of screened Zn formed, which instead exhibited a concomitant increase with higher loading level, suggests that its formation mechanism is a process that acts to deactivate whole volume sections of the plated anode, rather than being confined to a surface reaction by-product (Figure 2F, illustration inserts).

To further explore the root cause of this aging-induced screened Zn loss, XCT was employed to capture the formation process. A Zn/Ti pouch cell was examined *in situ* with its anode closely monitored while undergoing a full cycle of charging, aging, and discharging under a constant pressure (Figures 3A–3H). After cell assembly, the pristine anode had a clean surface (Figures 3A and 3E) with only a few sporadic bubbles on the Ti current collector that were trapped by the separator during assembly. This clean surface allowed a uniform Zn electrodeposition upon charging (Figures 3B and 3F). New gas bubbles started to form on the plated Zn right after charging (Figures 3B and 3F), which then gradually grew and merged into larger bubbles after 12 h of aging (Figures 3C and 3G). These bubbles were likely H_2 formed during the anode corrosion process outlined in Equation 3. Upon discharging (Figures 3D and 3H), most of the plated Zn was unaffected by the bubbles and could be completely stripped, re-exposing the underlying Ti current collector. However, parts of the plated-Zn anode, obscured underneath the larger bubbles, could not be stripped and became screened (Figure 3D, red arrows), resulting in the residual screened Zn that we observed coating the separator in Figure 2C.

This process is more prominent in cells at lower pressure and left for a longer aging time. A greater number of bubbles with a larger size could be seen across the anode surface after 48 h of aging, which resulted in significantly more screened Zn remaining on the anode surface following discharge (Figures 3I and 3K). From the cross-sections of the *in situ* tomography scans, the bubble-induced screened Zn formation process can be clearly visualized: During aging, bubbles formed, grew, and merged across the anode surface, physically displacing the electrolyte away from the plated Zn. These regions of the interface no longer had contact with the $ZnSO_4$ electrolyte (Figure 3J). As a result, during stripping, only those regions on the anode surface where the electrode-electrolyte contact was maintained were able to undergo dissolution (Figure 3L, green arrows), while those areas where bubbles displaced the electrolyte—breaking the interfacial contact and ionically insulating the plated Zn from

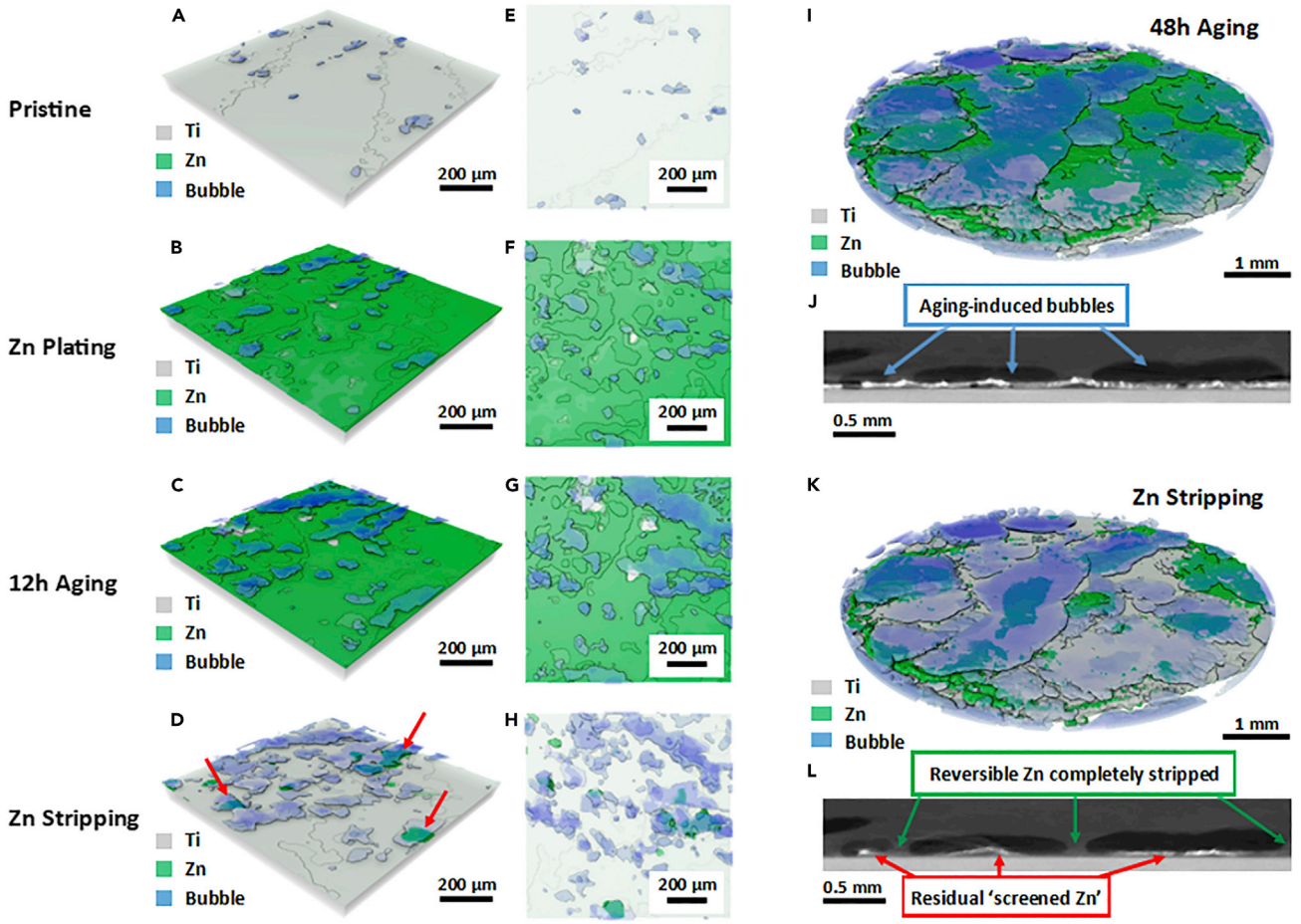

Figure 3. *In situ* XCT of Zn anodes undergoing aging

(A–H) The anode of a pressured Zn/Ti pouch cell scanned *in situ* using XCT, imaged through a full cycle of (A and E) pristine, (B and F) charging, (C and G) 12 h of aging, and (D and H) discharging. (A–D) 3D rendered images from a side-view angle and (E–H) from a top view.

(I–L) Anode of a pressure-free Zn/Ti pouch cell (I and J) after charging and 48 h of aging, and (K–L) after discharging. (I and K) 3D rendered images from side view; (J and L) cross-sections of the *in situ* tomography scans. Cells were charged and discharged at 10 mA cm^{-2} rate and had a 4 mAh cm^{-2} anode Zn loading.

the electrolyte—could not undergo stripping.[19] These screened areas of the anode were thus eventually left as residual screened Zn remnant on the Ti current collector (Figure 3L, red arrows), causing capacity loss. Longer aging leads to more H_2 evolution, promoting more bubble growth, while lower pressure results in higher bubble mobility, promoting bubble mergence into larger ones better able to screen the anode and thus increase screened Zn formation. This bubble accumulation on the Zn anode is not reversible, as the cell is sealed and the gas cannot be removed.[55] Over repeated cycles the accumulated bubbles will reduce the effective surface area of the Zn anode available for subsequent cycling due to physically displacing the electrolyte away from the anode, which, as well as causing the isolation of screened Zn, will also lead to localized points of high current density[49,50,56] during plating that will accelerate other anode issues like dendrite formation.

We also explored the role of any potential contribution to gas formation at the cathode side by XCT, performing both cycling and aging studies on a MnO_2/Zn full cell. Oxygen evolution occurs at the MnO_2 cathode during electrochemical cycling, as previously reported,[57] and could thus present a potential additional source of gas

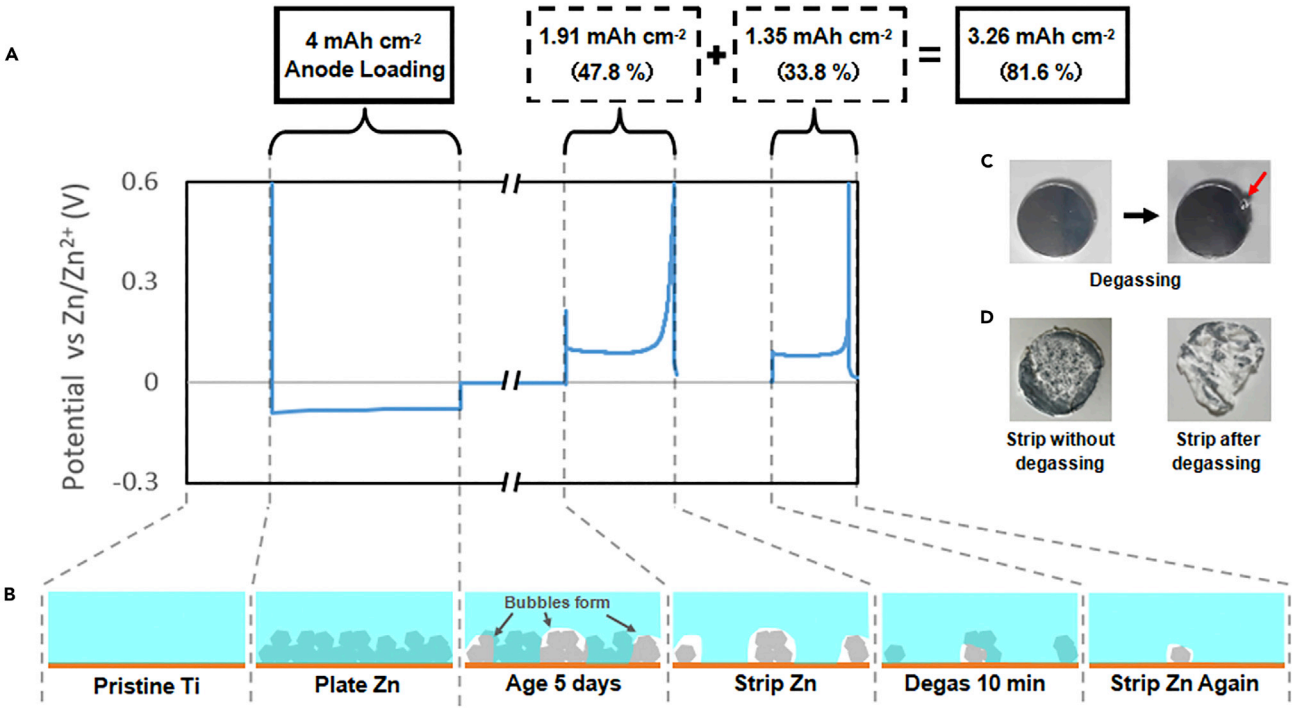

Figure 4. Capacity recovery by degassing

(A) The applied test sequence for a degassing test on a Zn/Ti coin cell, including anode Zn loading, 5 days of aging, initial electrostripping, degassing, and post-degassing electrostripping. The plated capacity was 4 mAh cm^{-2}, and the stripped capacities were 1.91 and 1.35 mAh cm^{-2}, respectively. Plating and stripping were at a rate of 10 mA cm^{-2}.

(B) Graphics illustrating the test sequence in (A).

(C) Optical images showing gas evolution from the cell during degassing (red arrow).

(D) Optical images showing reduced quantity of residual metallic Zn on the separator due to degassing.

accumulation in a full cell. However, our XCT imaging of the cathode revealed no detectable bubble formation due to aging or electrochemical cycling (Figure S10). This suggests that, compared with hydrogen formation at the Zn anode, oxygen evolution from the cathode side is unlikely to cause any cathode screening.

To further verify this model of screened Zn-induced anode capacity loss due to electrolyte displacement, and to more completely distinguish it from metallic Zn lost as dead Zn, a degassing test was performed on a coin cell following aging and stripping. After 120 h of aging, only 1.91 mAh cm^{-2} (CE = 47.8%) of the 4 mAh cm^{-2} plated Zn remained active (Figure 4A). The cell was then degassed in the electrolyte for 10 min to remove some of the H_2 bubbles accumulated on the Zn-anode surface (see experimental procedures). Without applying any external pressure, a continuous stream of bubbles escaping from the coin cell could be observed from the start of the degassing process (Figure 4; Video S1). After degassing, an extra discharge capacity of 1.35 mAh cm^{-2} could be retrieved from the cell, raising the overall cell's post-aging CE from 47.8% to 81.6%. Significantly less residual screened Zn was observed on the separator of the degassed cell (Figure 4D). This degassing test supports the notion that the formation mechanism of screened Zn is due to gas-bubble accumulation at the anode interface, displacing the electrolyte from parts of the Zn anode and impeding ionic transfer. Releasing the accumulated gas from the cell allowed for some restoration of the anode's capacity, as the expulsion of the gas restored the electrolyte-electrode interface and thus permitted unimpeded ionic flow to formerly screened Zn (Figure 4B). Similar capacity recovery was also observed

in MnO_2/Zn full cells (Figure S5) and with porous Zn anodes (Figure S11). By contrast, aging and degassing experiments conducted with 6 M KOH electrolyte, an alkaline electrolyte frequently used in zinc-air battery studies, exhibited minimal recovery following degassing (Figure S12), suggesting that the formation of corrosion products is instead the dominant source of anode capacity loss for such systems.

We performed several full-cell studies at various anode loading conditions to illustrate the relevance of anode aging to practical AZBs, thus highlighting the importance of this screened Zn mechanism when considering all the possible contributors to capacity loss (Figures S5 and S11). These full cell results demonstrate the importance of designing cells that can account for or minimize gas evolution. Using a flow-cell design would provide a route of egress for accumulated gas, in addition to the other benefits these cells can provide, such as electrolyte replenishment and convection control.[58,59] Alternatively, electrolyte combinations that are less susceptible to corrosion would reduce the volume of hydrogen evolved. For instance, we performed a simple comparison experiment between an aqueous and nonaqueous (organic) solvent electrolyte, with the latter expected to not undergo any analogous corrosion due to the lack of water. As well as showing much less aging loss (Figure S13A), the organic electrolyte cell suffered less volume expansion of the coin cell, suggesting less gas evolution (Figures S13B and S13C). The electrode itself could also be manipulated. Certain facets of zinc are known to be more resistant to corrosion; therefore, engineering anodes to exhibit more stable (002) facets should reduce aging-related performance decay.[60] Promoting a more uniform electroplating morphology and preventing dendrite formation will also reduce gas accumulation due to a smaller surface area of zinc being exposed to the corroding electrolyte.[61] Recent work has suggested that the nature of the solvation of zinc in the electrolyte may also provide a contribution toward hydrogen evolution, thus modifying the solvation structure with additives could prevent hydrogen formation.[62]

DISCUSSION

We have decoupled and quantified the Zn anode's aging-induced degradation in $ZnSO_4$-based AZBs with respect to different charging rates, anode loadings, and aging times. It was found that cell aging can lead to significant anode capacity loss, in some cases over 70% efficiency loss, after only 24 h of aging. This was aggravated by use of longer aging time, higher anode loading, and lower charging rates, and ultimately led to poor post-aging reversibility and short cell shelf life. While the loss was found to partly originate from the irreversible formation of zinc corrosion products like ZHS, it was mostly observed to be due to the presence of screened Zn, accounting for over 80% of the aging-capacity loss. Using *in situ* XCT, we revealed that the screened Zn formed due to gas-bubble formation and accumulation at the anode interface during aging. The trapped bubbles displaced the electrolyte from parts of the Zn anode, effectively leaving some regions ionically insulated from the electrolyte and thus unable to be dissolved during electrostripping; i.e., they were ionically screened during discharge. We demonstrated that by simply degassing the cells, these screened Zn can re-establish ionic connectivity with the electrolyte and thus restore a significant portion of the lost anode capacity.

By quantifying the aging contribution to capacity loss, decoupled from other contributors to capacity decay, we demonstrate the crucial importance of gas screening in deactivating zinc-metal anodes. Whereas prior works have observed bubble formation and hydrogen evolution as being part of the mix of degradation processes at the anode,[51,63–65] we hope that our quantitative diagnosis of its importance helps

stimulate further research into understanding and militating against this often overlooked source of capacity fade. Approaches to limit such gas formation, such as by applying a protective layer,[24,26,27,33,52,66–72] modifying the electrolyte,[25,33,73–75] using a solid/gel electrolyte to impede H_2 generation from corrosion[76–80] or by removing the formed H_2 by a flow cell or degassing[81,82] should be explored. Our work also highlights the importance of understanding the complex nature and interplay of the degradation processes that occur at the metal anode. Further investigation into the relationship this aging-induced screened Zn loss has with the electrolyte composition, electrolyte pH, and the formed corrosion products,[83–85] would help to illuminate additional strategies that may further combat capacity loss in metal anode AZBs.

EXPERIMENTAL PROCEDURES

Resource availability

Lead contact

Further information and requests for resources should be directed to and will be fulfilled by the lead contact, Alex Robertson (alex.w.robertson@warwick.ac.uk).

Materials availability

This study did not generate new unique reagents.

Data and code availability

The datasets generated and/or analyzed during the current study are available from the corresponding authors on reasonable request.

Material preparation

Glass fiber paper (0.26 mm thick), Ti foil (0.125 mm thick) and Zn Foil (0.25 mm and rolled to 0.18 mm thick) were purchased from Sigma Aldrich and were punctured into circular disks of 19 mm diameter (Glass fiber & Ti) and 16 mm diameter (Zn) to be used in the coin cells. All other LIR 2032-coin cell components were purchased from MTI Corporation. 2 M $ZnSO_4$ electrolyte was purchased from Sigma Aldrich. We prepared a porous Cu skeleton Zn anode as described in the literature[30]; in brief, a copper foil was cleaned in dilute hydrochloric acid then treated in 5 wt % NH_3 solution for 15 h to yield a copper foam. This was then electroplated with zinc to a capacity of 4 mAh cm^{-2} at 10 mA cm^{-2} from a 2 M $ZnSO_4$ solution. MnO_2 was synthesized by a solid state reaction between $KMnO_4$ (Sigma Aldrich) and $Mn(CH_3COO)_2{\cdot}4H_2O$ (Sigma Aldrich), with the stoichiometric ratio of $KMnO_4$: $Mn(CH_3COO)_2{\cdot}4H_2O$ = 2:3.[86]

Coin cell tests

All the aging quantification tests were performed using Zn/Ti cells as shown in Figure S1. Unless stated otherwise, tests were performed with 2 M $ZnSO_4$ electrolyte and with a standard Zn capacity loading of 4 mAh cm^{-2} and a cycling rate of 10 mA cm^{-2}. All cells were sealed and pressed to around 1,000 psi. The same current density was used during the charging stage and the discharging stage, i.e., plating and stripping. Each test was repeated with three coin cells to ensure consistency.

For the initial quantification tests (Figure 1), all the coin cells only used a single separator. For MS, XRD, optical tests, all cells used double separators and only the separator facing the anode was examined in these tests. This it to avoid detecting any possible products from side reactions at the counter electrode. 100 μL of electrolyte was used for each of the single-separator cell and 140 μL was used for each of the

double-separator cells, to make sure the separators were fully soaked and left minimal trapped air.

MnO_2 electrodes were prepared by mixing 80 wt % MnO_2, 10 wt % Super P carbon additive and 10 wt % polytetrafluoroethylene (PTFE) binder in mortar to form the freestanding film. The mass loading of MnO_2 electrode was controlled to about 6.3 mg cm^{-2}. The full cells were prepared by incorporating MnO_2 cathode, Zn foil anode, and separator with 2 M $ZnSO_4$ into a 2032 coin cell. Galvanostatic tests of the full cells were carried out at a current density of 200 mA g^{-1} with a Maccor Series 4000. All tests were performed at room temperature.

Degassing test

Degassing was performed by immerging an aged and discharged cell in $ZnSO_4$ electrolyte after a crack was deliberately made on the coin cell by grinding off its edge using a 400-grid grinding paper.

SUPPLEMENTAL INFORMATION

Supplemental information can be found online at https://doi.org/10.1016/j.joule.2023.01.010.

ACKNOWLEDGMENTS

The authors thank the support and acknowledge the use of the facilities of the DCCEM, at the Materials Department, Oxford (EP/R010145/1). P.G.B. is indebted to the Engineering and Physical Sciences Research Council (EPSRC), including the SUPERGEN Energy Storage Hub (EP/L019469/1), Enabling Next Generation Lithium Batteries (EP/M009521/1), Henry Royce Institute for Advanced Materials, and the Faraday for financial support. A.W.R. thanks the support of the Royal Society (UF160183). The XCT was facilitated by EPSRC grant EP/M02833X/1. The Zeiss Crossbeam FIB/SEM was supported by EPSRC grant EP/N010868/1.

AUTHOR CONTRIBUTIONS

S.D.P. conceived the idea and did the aging experiments. S.D.P., S.Z., and Z.N. designed the initial experiments. X.G., P.G.B., and A.W.R. directed the project and drafting the manuscript. B.H. and T.J.M. conducted and analyzed the XCT. Y.Y., C.G., J.Y., Z.L., and Y.T.T. performed aging experiments, SEM, EDS, and cell assembly. C.C. and S.Y. performed mass spectrometry. L.P. acquired the XRD.

DECLARATION OF INTERESTS

The authors declare no competing interests.

Received: July 22, 2022
Revised: August 24, 2022
Accepted: January 17, 2023
Published: February 15, 2023

REFERENCES

1. McLarnon, F.R., and Cairns, E.J. (1991). The secondary alkaline zinc electrode. J. Electrochem. Soc. *138*, 645–656. https://doi.org/10.1149/1.2085653.

2. Zhang, T., Tang, Y., Guo, S., Cao, X., Pan, A., Fang, G., Zhou, J., and Liang, S. (2020). Fundamentals and perspectives in developing zinc-ion battery electrolytes: a comprehensive review. Energy Environ. Sci. *13*, 4625–4665. https://doi.org/10.1039/D0EE02620D.

3. Song, M., Tan, H., Chao, D., and Fan, H.J. (2018). Recent advances in Zn-ion batteries. Adv. Funct. Mater. *28*, 1–27. https://doi.org/10.1002/adfm.201802564.

4. Liu, C., Xie, X., Lu, B., Zhou, J., and Liang, S. (2021). Electrolyte strategies toward better zinc-ion batteries. ACS Energy Lett. *6*, 1015–1033. https://doi.org/10.1021/acsenergylett.0c02684.

5. Lu, W., Zhang, C., Zhang, H., and Li, X. (2021). Anode for zinc-based batteries: challenges,

strategies, and prospects. ACS Energy Lett. *6*, 2765–2785. https://doi.org/10.1021/acsenergylett.1c00939.

6. Turney, D.E., Gallaway, J.W., Yadav, G.G., Ramirez, R., Nyce, M., Banerjee, S., Chen-Wiegart, Y.K., Wang, J., D'Ambrose, M.J., Kolhekar, S., et al. (2017). Rechargeable zinc alkaline anodes for long-cycle energy storage. Chem. Mater. *29*, 4819–4832. https://doi.org/10.1021/acs.chemmater.7b00754.

7. Shoji, T., Hishinuma, M., and Yamamoto, T. (1988). Zinc-manganese dioxide galvanic cell using zinc sulphate as electrolyte. Rechargeability of the cell. J. Appl. Electrochem. *18*, 521–526. https://doi.org/10.1007/BF01022245.

8. Pan, H., Shao, Y., Yan, P., Cheng, Y., Han, K.S., Nie, Z., Wang, C., Yang, J., Li, X., Bhattacharya, P., et al. (2016). Reversible aqueous zinc/manganese oxide energy storage from conversion reactions. Nat. Energy *1*, 16039. https://doi.org/10.1038/nenergy.2016.39.

9. Kundu, D., Adams, B.D., Duffort, V., Vajargah, S.H., and Nazar, L.F. (2016). A high-capacity and long-life aqueous rechargeable zinc battery using a metal oxide intercalation cathode. Nat. Energy *1*, 16119. https://doi.org/10.1038/nenergy.2016.119.

10. Ma, L., Chen, S., Li, H., Ruan, Z., Tang, Z., Liu, Z., Wang, Z., Huang, Y., Pei, Z., Zapien, J.A., and Zhi, C. (2018). Initiating a mild aqueous electrolyte Co_3O_4/Zn battery with 2.2 V-high voltage and 5000-cycle lifespan by a Co(iii) rich-electrode. Energy Environ. Sci. *11*, 2521–2530. https://doi.org/10.1039/C8EE01415A.

11. Yang, J., Yin, B., Sun, Y., Pan, H., Sun, W., Jia, B., Zhang, S., and Ma, T. (2022). Zinc anode for mild aqueous zinc-ion batteries: challenges, strategies, and perspectives. Nanomicro Lett. *14*, 42. https://doi.org/10.1007/s40820-021-00782-5.

12. Yang, G., Huang, J., Wan, X., Liu, B., Zhu, Y., Wang, J., Fontaine, O., Luo, S., Hiralal, P., Guo, Y., and Zhou, H. (2022). An aqueous zinc-ion battery working at −50°C enabled by low-concentration perchlorate-based chaotropic salt electrolyte. Ecomat. *4*, e12165. https://doi.org/10.1002/eom2.12165.

13. Shi, Y., Chen, Y., Shi, L., Wang, K., Wang, B., Li, L., Ma, Y., Li, Y., Sun, Z., Ali, W., and Ding, S. (2020). An overview and future perspectives of rechargeable zinc batteries. Small *16*, e2000730. https://doi.org/10.1002/smll.202000730.

14. Huang, J., Guo, Z., Ma, Y., Bin, D., Wang, Y., and Xia, Y. (2019). Recent progress of rechargeable batteries using mild aqueous electrolytes. Small Methods *3*, 1800272. https://doi.org/10.1002/smtd.201800272.

15. Verma, V., Kumar, S., Manalastas, W., and Srinivasan, M. (2021). Undesired reactions in aqueous rechargeable zinc ion batteries. ACS Energy Lett. *6*, 1773–1785. https://doi.org/10.1021/acsenergylett.1c00393.

16. Hao, J., Li, X., Zeng, X., Li, D., Mao, J., and Guo, Z. (2020). Deeply understanding the Zn anode behaviour and corresponding improvement strategies in different aqueous Zn-based batteries. Energy Environ. Sci. *13*, 3917–3949. https://doi.org/10.1039/D0EE02162H.

17. Yang, Q., Li, Q., Liu, Z., Wang, D., Guo, Y., Li, X., Tang, Y., Li, H., Dong, B., and Zhi, C. (2020). Dendrites in Zn-based batteries. Adv. Mater. *32*, e2001854. https://doi.org/10.1002/adma.202001854.

18. Li, C., Xie, X., Liang, S., and Zhou, J. (2020). Issues and future perspective on zinc metal anode for rechargeable aqueous zinc-ion batteries. Energy Environ. Mater. *3*, 146–159. https://doi.org/10.1002/eem2.12067.

19. Xie, C., Li, Y., Wang, Q., Sun, D., Tang, Y., and Wang, H. (2020). Issues and solutions toward zinc anode in aqueous zinc-ion batteries: a mini review. Carbon Energy *2*, 540–560. https://doi.org/10.1002/cey2.67.

20. Tang, B., Shan, L., Liang, S., and Zhou, J. (2019). Issues and opportunities facing aqueous zinc-ion batteries. Energy Environ. Sci. *12*, 3288–3304. https://doi.org/10.1039/C9EE02526J.

21. Blanc, L.E., Kundu, D., and Nazar, L.F. (2020). Scientific challenges for the implementation of Zn-ion batteries. Joule *4*, 771–799. https://doi.org/10.1016/j.joule.2020.03.002.

22. Hoang Huy, V.P.H., Hieu, L.T., and Hur, J. (2021). Zn metal anodes for Zn-ion batteries in mild aqueous electrolytes: challenges and strategies. Nanomaterials (Basel) *11*, 2746. https://doi.org/10.3390/nano11102746.

23. Cai, Z., Wang, J., Lu, Z., Zhan, R., Ou, Y., Wang, L., Dahbi, M., Alami, J., Lu, J., Amine, K., and Sun, Y. (2022). Ultrafast metal electrodeposition revealed by in situ optical imaging and theoretical modeling towards fast-charging Zn battery chemistry. Angew. Chem. Int. Ed. Engl. *61*, e202116560. https://doi.org/10.1002/anie.202116560.

24. Hoang, T.K.A., Doan, T.N.L., Sun, K.E.K., and Chen, P. (2015). Corrosion chemistry and protection of zinc & zinc alloys by polymer-containing materials for potential use in rechargeable aqueous batteries. RSC Adv. *5*, 41677–41691. https://doi.org/10.1039/C5RA00594A.

25. Wang, F., Borodin, O., Gao, T., Fan, X., Sun, W., Han, F., Faraone, A., Dura, J.A., Xu, K., and Wang, C. (2018). Highly reversible zinc metal anode for aqueous batteries. Nat. Mater. *17*, 543–549. https://doi.org/10.1038/s41563-018-0063-z.

26. Ma, L., Li, Q., Ying, Y., Ma, F., Chen, S., Li, Y., Huang, H., and Zhi, C. (2021). Toward practical high-areal-capacity aqueous zinc-metal batteries: quantifying hydrogen evolution and a solid-ion conductor for stable zinc anodes. Adv. Mater. *33*, e2007406. https://doi.org/10.1002/adma.202007406.

27. Deng, C., Xie, X., Han, J., Tang, Y., Gao, J., Liu, C., Shi, X., Zhou, J., and Liang, S. (2020). A sieve-functional and uniform-porous kaolin layer toward stable zinc metal anode. Adv. Funct. Mater. *30*, 2000599. https://doi.org/10.1002/adfm.202000599.

28. Hao, J., Li, X., Zhang, S., Yang, F., Zeng, X., Zhang, S., Bo, G., Wang, C., and Guo, Z. (2020). Designing dendrite-free zinc anodes for advanced aqueous zinc batteries. Adv. Funct. Mater. *30*, 2001263. https://doi.org/10.1002/adfm.202001263.

29. Parker, J.F., Chervin, C.N., Nelson, E.S., Rolison, D.R., and Long, J.W. (2014). Wiring zinc in three dimensions re-writes battery performance - dendrite-free cycling. Energy Environ. Sci. *7*, 1117–1124. https://doi.org/10.1039/C3EE43754J.

30. Kang, Z., Wu, C., Dong, L., Liu, W., Mou, J., Zhang, J., Chang, Z., Jiang, B., Wang, G., Kang, F., and Xu, C. (2019). 3D porous copper skeleton supported zinc anode toward high capacity and long cycle life zinc ion batteries. ACS Sustainable Chem. Eng. *7*, 3364–3371. https://doi.org/10.1021/acssuschemeng.8b05568.

31. Xiong, P., Kang, Y., Yuan, H., Liu, Q., Baek, S.H., Park, J.M., Dou, Q., Han, X., Jang, W.S., Kwon, S.J., et al. (2022). Galvanically replaced artificial interfacial layer for highly reversible zinc metal anodes. Appl. Phys. Rev. *9*, 011401. https://doi.org/10.1063/5.0074327.

32. Han, D., Cui, C., Zhang, K., Wang, Z., Gao, J., Guo, Y., Zhang, Z., Wu, S., Yin, L., Weng, Z., et al. (2022). A non-flammable hydrous organic electrolyte for sustainable zinc batteries. Nat. Sustain. *5*, 205–213. https://doi.org/10.1038/s41893-021-00800-9.

33. Guo, X., Zhang, Z., Li, J., Luo, N., Chai, G.-L., Miller, T.S., Lai, F., Shearing, P., Brett, D.J.L., Han, D., et al. (2021). Alleviation of dendrite formation on zinc anodes via electrolyte additives. ACS Energy Lett. *6*, 395–403. https://doi.org/10.1021/acsenergylett.0c02371.

34. Liu, Z., Cui, T., Pulletikurthi, G., Lahiri, A., Carstens, T., Olschewski, M., and Endres, F. (2016). Dendrite-free nanocrystalline zinc electrodeposition from an ionic liquid containing nickel triflate for rechargeable Zn-based batteries. Angew. Chem. Int. Ed. Engl. *55*, 2889–2893. https://doi.org/10.1002/anie.201509364.

35. Yuan, D., Zhao, J., Ren, H., Chen, Y., Chua, R., Jie, E.T.J., Cai, Y., Edison, E., Manalastas, W., Wong, M.W., and Srinivasan, M. (2021). Anion texturing towards dendrite-free Zn anode for aqueous rechargeable batteries. Angew. Chem. Int. Ed. Engl. *60*, 7213–7219. https://doi.org/10.1002/anie.202015488.

36. Zhou, M., Guo, S., Li, J., Luo, X., Liu, Z., Zhang, T., Cao, X., Long, M., Lu, B., Pan, A., et al. (2021). Surface-preferred crystal plane for a stable and reversible zinc anode. Adv. Mater. *33*, e2100187. https://doi.org/10.1002/adma.202100187.

37. Zheng, J., and Archer, L.A. (2021). Controlling electrochemical growth of metallic zinc electrodes: toward affordable rechargeable energy storage systems. Sci. Adv. *7*, eabe0219. https://doi.org/10.1126/sciadv.abe0219.

38. Foroozan, T., Yurkiv, V., Sharifi-Asl, S., Rojaee, R., Mashayek, F., and Shahbazian-Yassar, R. (2019). Non-dendritic Zn electrodeposition enabled by Zincophilic graphene substrates. ACS Appl. Mater. Interfaces *11*, 44077–44089. https://doi.org/10.1021/acsami.9b13174.

39. Zampardi, G., and La Mantia, F. (2022). Open challenges and good experimental practices in the research field of aqueous Zn-ion batteries. Nat. Commun. *13*, 687. https://doi.org/10.1038/s41467-022-28381-x.

40. Ma, L., Schroeder, M.A., Borodin, O., Pollard, T.P., Ding, M.S., Wang, C., and Xu, K. (2020). Realizing high zinc reversibility in rechargeable

batteries. Nat. Energy *5*, 743–749. https://doi.org/10.1038/s41560-020-0674-x.

41. Qian, J., Henderson, W.A., Xu, W., Bhattacharya, P., Engelhard, M., Borodin, O., and Zhang, J.G. (2015). High rate and stable cycling of lithium metal anode. Nat. Commun. *6*, 6362. https://doi.org/10.1038/ncomms7362.

42. Xiao, J., Li, Q., Bi, Y., Cai, M., Dunn, B., Glossmann, T., Liu, J., Osaka, T., Sugiura, R., Wu, B., et al. (2020). Understanding and applying coulombic efficiency in lithium metal batteries. Nat. Energy *5*, 561–568. https://doi.org/10.1038/s41560-020-0648-z.

43. Adams, B.D., Zheng, J., Ren, X., Xu, W., and Zhang, J.G. (2018). Accurate determination of coulombic efficiency for lithium metal anodes and lithium metal batteries. Adv. Energy Mater. *8*, 1702097. https://doi.org/10.1002/aenm.201702097.

44. Sagüés, A.A., and Powers, R.G. (1996). Sprayed-zinc sacrificial anodes for reinforced concrete in marine service. Corrosion *52*, 508–522. https://doi.org/10.5006/1.3292141.

45. Farooq, A., Hamza, M., Ahmed, Q., and Deen, K.M. (2019). Evaluating the performance of zinc and aluminum sacrificial anodes in artificial seawater. Electrochim. Acta *314*, 135–141. https://doi.org/10.1016/j.electacta.2019.05.067.

46. Wang, H., Du, M., Liang, H., and Gao, Q. (2019). Study on Al-Zn-in alloy as sacrificial anodes in seawater environment. J. Ocean Univ. China *18*, 889–895. https://doi.org/10.1007/s11802-019-3788-7.

47. Sadawy, M., Saad, S., and Abdel-Karim, R. (2020). Effect of Zn/Mg ratio on cathodic protection of carbon steel using Al−Zn−Mg sacrificial anodes. Trans. Nonferrous Met. Soc. China Engl. Ed. *30*, 2067–2078. https://doi.org/10.1016/S1003-6326(20)65361-4.

48. Glatz, H., Tervoort, E., and Kundu, D. (2020). Unveiling critical insight into the Zn metal anode cyclability in mildly acidic aqueous electrolytes: implications for aqueous zinc batteries. ACS Appl. Mater. Interfaces *12*, 3522–3530. https://doi.org/10.1021/acsami.9b16125.

49. Yang, Q., Liang, G., Guo, Y., Liu, Z., Yan, B., Wang, D., Huang, Z., Li, X., Fan, J., and Zhi, C. (2019). Do zinc dendrites exist in neutral zinc batteries: a developed electrohealing strategy to in situ rescue in-service batteries. Adv. Mater. *31*, e1903778. https://doi.org/10.1002/adma.201903778.

50. Gao, X., Zhou, Y.N., Han, D., Zhou, J., Zhou, D., Tang, W., and Goodenough, J.B. (2020). Thermodynamic understanding of Li-dendrite formation. Joule *4*, 1864–1879. https://doi.org/10.1016/j.joule.2020.06.016.

51. Yufit, V., Tariq, F., Eastwood, D.S., Biton, M., Wu, B., Lee, P.D., and Brandon, N.P. (2019). Operando visualization and multi-scale tomography studies of dendrite formation and dissolution in zinc batteries. Joule *3*, 485–502. https://doi.org/10.1016/j.joule.2018.11.002.

52. Hao, J., Li, B., Li, X., Zeng, X., Zhang, S., Yang, F., Liu, S., Li, D., Wu, C., and Guo, Z. (2020). An in-depth study of Zn metal surface chemistry for advanced aqueous Zn-ion batteries. Adv. Mater. *32*, e2003021. https://doi.org/10.1002/adma.202003021.

53. Zhang, Y., Yang, G., Lehmann, M.L., Wu, C., Zhao, L., Saito, T., Liang, Y., Nanda, J., and Yao, Y. (2021). Separator effect on zinc electrodeposition behavior and its implication for zinc battery lifetime. Nano Lett. *21*, 10446–10452. https://doi.org/10.1021/acs.nanolett.1c03792.

54. Zuo, Y., Wang, K., Pei, P., Wei, M., Liu, X., Xiao, Y., and Zhang, P. (2021). Zinc dendrite growth and inhibition strategies. Mater. Today Energy *20*, 100692. https://doi.org/10.1016/j.mtener.2021.100692.

55. Cai, Z., Ou, Y., Wang, J., Xiao, R., Fu, L., Yuan, Z., Zhan, R., and Sun, Y. (2020). Chemically resistant Cu–Zn/Zn composite anode for long cycling aqueous batteries. Energy Storage Mater. *27*, 205–211. https://doi.org/10.1016/j.ensm.2020.01.032.

56. Pu, S.D., Gong, C., Gao, X., Ning, Z., Yang, S., Marie, J.J., Liu, B., House, R.A., Hartley, G.O., Luo, J., et al. (2020). Current-density-dependent electroplating in Ca electrolytes: from globules to dendrites. ACS Energy Lett. *5*, 2283–2290. https://doi.org/10.1021/acsenergylett.0c01153.

57. Shen, X., Wang, X., Zhou, Y., Shi, Y., Zhao, L., Jin, H., Di, J., and Li, Q. (2021). Highly reversible aqueous Zn-MnO_2 battery by supplementing Mn^{2+}-Mediated MnO_2 deposition and dissolution. Adv. Funct. Mater. *31*, 2101579. https://doi.org/10.1002/adfm.202101579.

58. Liu, Y., Lu, X., Lai, F., Liu, T., Shearing, P.R., Parkin, I.P., He, G., and Brett, D.J.L. (2021). Rechargeable aqueous Zn-based energy storage devices. Joule *5*, 2845–2903. https://doi.org/10.1016/j.joule.2021.10.011.

59. Liu, W., Lu, W., Zhang, H., and Li, X. (2019). Aqueous flow batteries: Research and Development. Chemistry *25*, 1649–1664. https://doi.org/10.1002/chem.201802798.

60. Zheng, J., and Archer, L.A. (2022). Crystallographically textured electrodes for rechargeable batteries: symmetry, fabrication, and characterization. Chem. Rev. *122*, 14440–14470. https://doi.org/10.1021/acs.chemrev.2c00022.

61. Pu, S.D., Gong, C., Tang, Y.T., Ning, Z., Liu, J., Zhang, S., Yuan, Y., Melvin, D., Yang, S., Pi, L., et al. (2022). Achieving ultrahigh-rate planar and dendrite-free zinc electroplating for aqueous zinc battery anodes. Adv. Mater. *34*, e2202552. https://doi.org/10.1002/adma.202202552.

62. Yang, F., Yuwono, J.A., Hao, J., Long, J., Yuan, L., Wang, Y., Liu, S., Fan, Y., Zhao, S., Davey, K., et al. (2022). Understanding H_2 evolution electrochemistry to minimize solvated water impact on zinc-anode performance. Adv. Mater. *34*, e2206754. https://doi.org/10.1002/adma.202206754.

63. Li, Q., Wang, Y., Mo, F., Wang, D., Liang, G., Zhao, Y., Yang, Q., Huang, Z., and Zhi, C. (2021). Calendar life of Zn batteries based on Zn anode with Zn powder/current collector structure. Adv. Energy Mater. *11*, 2003931. https://doi.org/10.1002/aenm.202003931.

64. Wang, H., Li, H., Tang, Y., Xu, Z., Wang, K., Li, Q., He, B., Liu, Y., Ge, M., Chen, S., et al. (2022). Stabilizing Zn anode interface by simultaneously manipulating the thermodynamics of Zn nucleation and overpotential of hydrogen evolution. Adv. Funct. Mater. *32*, 2207898. https://doi.org/10.1002/adfm.202207898.

65. Bani Hashemi, A., Kasiri, G., and La Mantia, F. (2017). The effect of polyethyleneimine as an electrolyte additive on zinc electrodeposition mechanism in aqueous zinc-ion batteries. Electrochim. Acta *258*, 703–708. https://doi.org/10.1016/j.electacta.2017.11.116.

66. Yuan, D., Manalastas, W., Zhang, L., Chan, J.J., Meng, S., Chen, Y., and Srinivasan, M. (2019). Lignin@Nafion membranes forming Zn solid–electrolyte interfaces enhance the cycle life for rechargeable zinc-ion batteries. ChemSusChem *12*, 4889–4900. https://doi.org/10.1002/cssc.201901409.

67. Zhao, Z., Zhao, J., Hu, Z., Li, J., Li, J., Zhang, Y., Wang, C., and Cui, G. (2019). Long-life and deeply rechargeable aqueous Zn anodes enabled by a multifunctional brightener-inspired interphase. Energy Environ. Sci. *12*, 1938–1949. https://doi.org/10.1039/C9EE00596J.

68. Xie, X., Liang, S., Gao, J., Guo, S., Guo, J., Wang, C., Xu, G., Wu, X., Chen, G., and Zhou, J. (2020). Manipulating the ion-transfer kinetics and interface stability for high-performance zinc metal anodes. Energy Environ. Sci. *13*, 503–510. https://doi.org/10.1039/C9EE03545A.

69. He, H., Qin, H., Wu, J., Chen, X., Huang, R., Shen, F., Wu, Z., Chen, G., Yin, S., and Liu, J. (2021). Engineering interfacial layers to enable Zn metal anodes for aqueous zinc-ion batteries. Energy Storage Mater. *43*, 317–336. https://doi.org/10.1016/j.ensm.2021.09.012.

70. Guo, J., Ming, J., Lei, Y., Zhang, W., Xia, C., Cui, Y., and Alshareef, H.N. (2019). Artificial solid electrolyte interphase for suppressing surface reactions and cathode dissolution in aqueous zinc ion batteries. ACS Energy Lett. *4*, 2776–2781. https://doi.org/10.1021/acsenergylett.9b02029.

71. Zhao, K., Wang, C., Yu, Y., Yan, M., Wei, Q., He, P., Dong, Y., Zhang, Z., Wang, X., and Mai, L. (2018). Ultrathin surface coating enables stabilized zinc metal anode. Adv. Mater. Interfaces *5*, 1800848. https://doi.org/10.1002/admi.201800848.

72. Han, D., Wu, S., Zhang, S., Deng, Y., Cui, C., Zhang, L., Long, Y., Li, H., Tao, Y., Weng, Z., et al. (2020). A corrosion-resistant and dendrite-free zinc metal anode in aqueous systems. Small *16*, e2001736. https://doi.org/10.1002/smll.202001736.

73. Guo, S., Qin, L., Zhang, T., Zhou, M., Zhou, J., Fang, G., and Liang, S. (2021). Fundamentals and perspectives of electrolyte additives for aqueous zinc-ion batteries. Energy Storage Mater. *34*, 545–562. https://doi.org/10.1016/j.ensm.2020.10.019.

74. Li, Y., Wu, P., Zhong, W., Xie, C., Xie, Y., Zhang, Q., Sun, D., Tang, Y., and Wang, H. (2021). A progressive nucleation mechanism enables stable zinc stripping-plating behavior. Energy Environ. Sci. *14*, 5563–5571. https://doi.org/10.1039/D1EE01861B.

75. Aurbach, D., and Gofer, Y. (1991). The behavior of lithium electrodes in mixtures of alkyl carbonates and ethers. J. Electrochem. Soc. *138*, 3529–3536. https://doi.org/10.1149/1.2085454.

76. Han, Q., Chi, X., Zhang, S., Liu, Y., Zhou, B., Yang, J., and Liu, Y. (2018). Durable, flexible self-standing hydrogel electrolytes enabling high-safety rechargeable solid-state zinc metal batteries. J. Mater. Chem. A *6*, 23046–23054. https://doi.org/10.1039/C8TA08314B.

77. Han, Q., Chi, X., Liu, Y., Wang, L., Du, Y., Ren, Y., and Liu, Y. (2019). An inorganic salt reinforced Zn^{2+}-conducting solid-state electrolyte for ultra-stable Zn metal batteries. J. Mater. Chem. A *7*, 22287–22295. https://doi.org/10.1039/C9TA07218G.

78. Wang, B., Li, J., Hou, C., Zhang, Q., Li, Y., and Wang, H. (2020). Stable hydrogel electrolytes for flexible and submarine-use Zn-ion batteries. ACS Appl. Mater. Interfaces *12*, 46005–46014. https://doi.org/10.1021/acsami.0c12313.

79. Zhang, H., Liu, X., Li, H., Qin, B., and Passerini, S. (2020). High-voltage operation of a V2O5 cathode in a concentrated gel polymer electrolyte for high-energy aqueous zinc batteries. ACS Appl. Mater. Interfaces *12*, 15305–15312. https://doi.org/10.1021/acsami.0c02102.

80. Ma, L., Chen, S., Li, N., Liu, Z., Tang, Z., Zapien, J.A., Chen, S., Fan, J., and Zhi, C. (2020). Hydrogen-free and dendrite-free all-solid-state Zn-ion batteries. Adv. Mater. *32*, e1908121. https://doi.org/10.1002/adma.201908121.

81. Zhang, H. (2019). Progress and perspectives of flow battery technologies. Curr. Opin. Electrochem. *18*, 123–125. https://doi.org/10.1016/j.coelec.2019.10.015.

82. Ruan, P., Liang, S., Lu, B., Fan, H.J., and Zhou, J. (2022). Design strategies for high-energy-density aqueous zinc batteries. Angew. Chem. Int. Ed. Engl. *61*, e202200598. https://doi.org/10.1002/anie.202200598.

83. Zhou, X., Lu, Y., Zhang, Q., Miao, L., Zhang, K., Yan, Z., Li, F., and Chen, J. (2020). Exploring the interfacial chemistry between zinc anodes and aqueous electrolytes via an in situ visualized characterization system. ACS Appl. Mater. Interfaces *12*, 55476–55482. https://doi.org/10.1021/acsami.0c17023.

84. Ji, Y., Yin, Z.-W., Yang, Z., Deng, Y.P., Chen, H., Lin, C., Yang, L., Yang, K., Zhang, M., Xiao, Q., et al. (2021). From bulk to interface: electrochemical phenomena and mechanism studies in batteries via electrochemical quartz crystal microbalance. Chem. Soc. Rev. *50*, 10743–10763. https://doi.org/10.1039/d1cs00629k.

85. Wittman, R.M., Sacci, R.L., and Zawodzinski, T.A. (2019). Elucidating mechanisms of oxide growth and surface passivation on zinc thin film electrodes in alkaline solutions using the electrochemical quartz crystal microbalance. J. Power Sources *438*, 227034. https://doi.org/10.1016/j.jpowsour.2019.227034.

86. Alfaruqi, M.H., Islam, S., Gim, J., Song, J., Kim, S., Pham, D.T., Jo, J., Xiu, Z., Mathew, V., and Kim, J.A. (2016). High surface area tunnel-type α-MnO_2 nanorod cathode by a simple solvent-free synthesis for rechargeable aqueous zinc-ion batteries. Chem. Phys. Lett. *650*, 64–68. https://doi.org/10.1016/j.cplett.2016.02.067.